Experimental and theoretical investigation of (*E*)-5-{[4-(dimethylamino)benzylidene]amino}-1,3,4-thiadiazole-2(3*H*)-thione (DATT) as an acid corrosion inhibitor of mild steel

M.D. Plotnikova, A.B. Shein, M.G. Scherban, A.N. Vasyanin and A.E. Rubtsov

Perm State National Research University, st. Bukireva 15, 614068, Perm, Russian Federation
*E-mail: plotnikova-md@mail.ru

Abstract

(*E*)-5-{[4-(Dimethylamino)benzylidene]amino}-1,3,4-thiadiazole-2(3*H*)-thione (DATT) was synthesized and its corrosion inhibitive efficiency on mild steel has been investigated in 1 and 5 mol L^{-1} HCl medium by gravimetric and electrochemical measurements. The structure of DATT was determined by Nuclear Magnetic Resonance (NMR) spectroscopy and Grimme's GFN2-xTB method. The same calculations determined that there are three most stable DATT protomers among mono, double and triple protonated structures. Fukui functions mapped on the van der Waals (vdW) surfaces of DBT and its protonated forms at the PBE0-D3BJ[C-PCM(Water)]/ma-def2-TZVP level of theory was determined. The polarization measurements and analysis of anodic and cathodic slopes of polarization curves have shown that DATT is a mixed-type inhibitor in HCl media in a broad temperature range. Scanning electron microscopy and surface profilometry confirmed the formation of protective films on mild steel surface. The inhibition efficiency of DATT is associated with the protonation of its molecules and increases with concentration of hydrochloric acid solutions when oxygen, sulfur and nitrogen atoms with their single electron pairs bind more easily to the free 3d orbitals of iron. The degree of steel coverage in 5 M HCl is higher than in 1 M acid, according to electrochemical impedance spectroscopy results. Contact angle measurement detected the hydrophobic nature of the steel surface modified by the inhibitor molecules applied in corrosive solutions. The influence of molecular configuration on the corrosion inhibition behavior of (*E*)-5-{[4-(dimethylamino)-benzylidene]dmino}-1,3,4-thiadiazole-2(3*H*)-thione was explored by quantum chemical calculation and MD simulation.

1. Introduction

Though alternatives to fossil fuels are now being investigated, the need of the mankind for them continues to grow. A decrease in oil production due to flowline blockage presents a

reason for oil well stimulation which in most cases involves the introduction of an acid to the oil well reservoir to dissolve formation rocks and/or soluble components present in the well [1]. The acidizing process encourages the corrosion of metallic components of oil wells and the acidizing equipment. Corrosion calls for a continuous search for better, more effective and ecologically friendly corrosion inhibitors. Hence, the employment of corrosion inhibitors to attain a balance between the boosting of the oil flow and protecting equipment from the aggressiveness of HCl is strongly required [2, 3]. During the past decades, organic heterocycles have been extensively used as corrosion inhibitors. Thiadiazoles, as a type of organic heterocycles, contain nitrogen and sulfur heteroatoms and multiple bonds, which allow adsorption on the metal surface [4–6]. This phenomenon is affected by the metal nature and surface charge, media, and chemical structure of inhibitors [7]. It has been observed that the adsorption of organic inhibitors depends on the electron density of the molecule's active parts, such as aromatic rings and heteroatoms [8–10]. Effective inhibitors were chosen using the empirical knowledge based on their physicochemical properties, mechanism of action, and electron-donating ability [8, 9]. Moreover, the selection of inhibitors is also determined by semi-empirical quantum chemical calculations by correlating the experimental data with quantum-chemical properties. The highest occupied molecular orbital (HOMO), lowest unoccupied molecular orbital (LUMO), charges on the reactive center, and conformations of molecules have been used to achieve the appropriate correlations [11, 12].

In our previous studies, we studied thiazole and thiadiazole derivatives as corrosion inhibitors for mild steel in HCl and H_2SO_4 solutions [13, 14]. We found that these compounds were effective inhibitors under these conditions. (*E*)-5-{[4-(Dimethylamino)-benzylidene]amino}-1,3,4-thiadiazole-2-thiol shows the best inhibiting results, and we are trying to study it in more detail. The aim of this work is to combine experimental and theoretical approaches to study (*E*)-5-{[4-(**D**imethylamino)benzylidene]**A**mino}-1,3,4-**T**hiadiazole-2(3*H*)-**T**hione (**DATT**) as a corrosion inhibitor in hydrochloric acid solutions.

2. Experimental Details

2.1. Synthesis of DATT

DATT was synthesized from 4-dimethylaminobenzylidehyde and 5-amino-1,3,4-thiadiazole-2-thiol by a simple one-step method, as shown in Scheme 1. Specifically, to a solution of 5-amino-1,3,4-thiadiazole-2-thiol (10 mmol) and 4-(dimethylamino)-benzylidehyde (10 mmol) in methanol (30 mL) was added a catalytic amount of concentrated hydrochloric acid (0.1 mL). The reaction mixture was heated at reflux temperature for 3 h, then kept overnight at room temperature. The precipitated solid was filtered off, washed with methanol, recrystallized from methanol, and dried *in vacuo* to give the DATT. Yield 92%, orange solid, m.p. 214–218°C. ^{1}H HMR (400 MHz, DMSO-d_6), δ: 3.06 (s, 6H), 6.80 (AA′BB′, 2H), 7.78 (AA′BB′, 2H), 8.39 (s, 1H), 14.19 (s, 1H). ^{13}C HMR (126 MHz, DMSO-d_6), δ: 111.5, 121.1, 132.2, 153.9, 165.7, 166.9, 185.7.

Int. J. Corros. Scale Inhib., 2023, **12**, no. 4, 1365–1391

1367
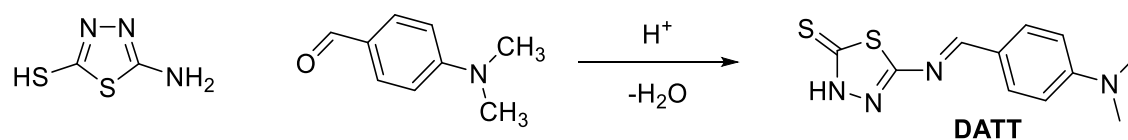
Scheme 1. Synthesis of (*E*)-5-{[4-(dimethylamino)benzylidene]amino}-1,3,4-thiadiazole-2(3*H*)-thione (DATT).
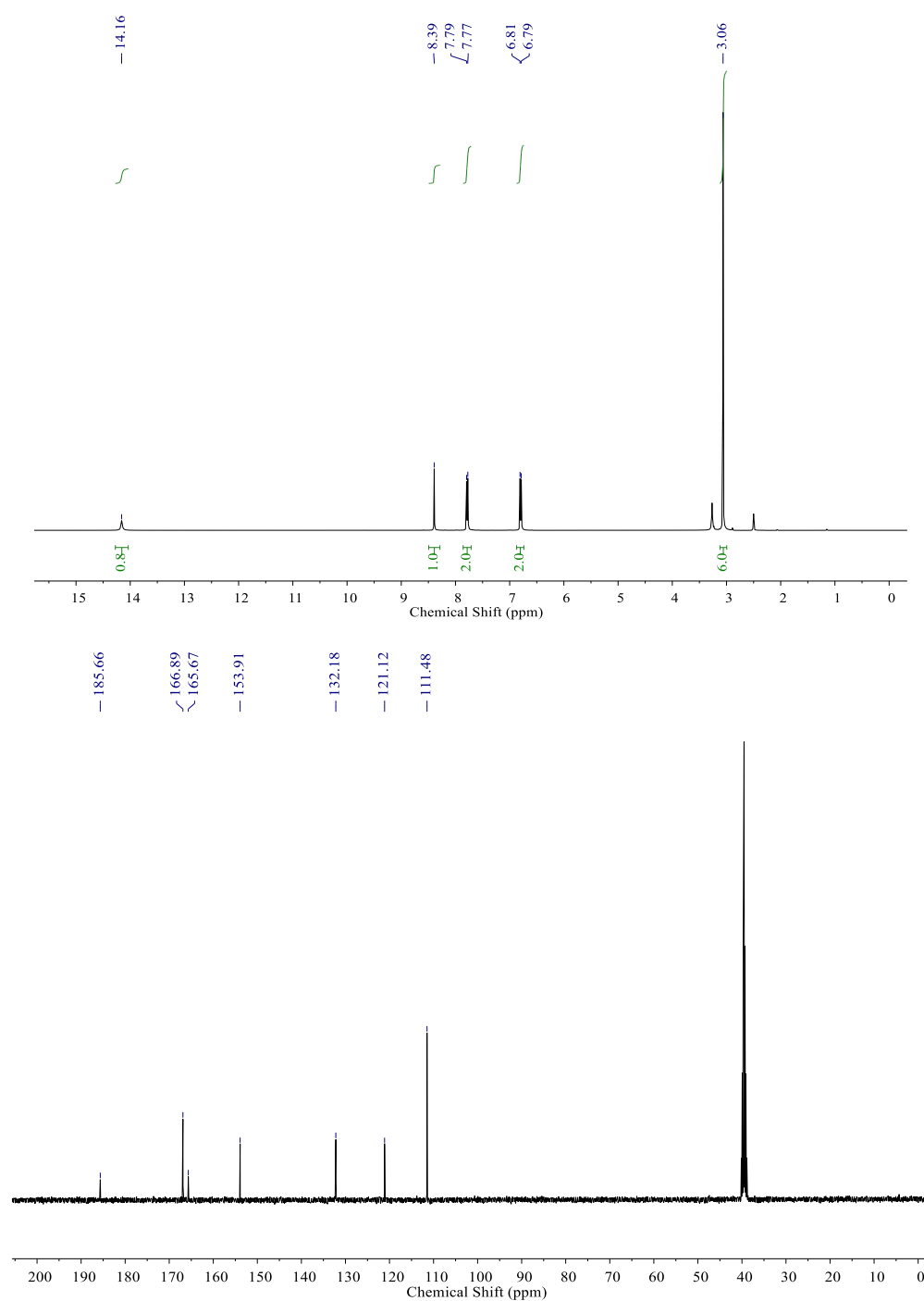

Figure 1. ^{1}H (a) and ^{13}C NMR spectra of DATT.

2.2. Specimens and solution

All experiments were carried out on AISI C1018 mild steel, which was cut into coupons of 25 mm×20 mm×2 mm dimensions for weight loss tests. Table 1 lists the chemical composition of C1018 steel.

Table 1. Chemical composition of the admixtures in the steel used in this study (wt.%).

Composition	C	Mn	P	S
wt.%	0.15–0.2	0.6–0.9	≤ 0.04	≤ 0.05

To perform electrochemical experiments, the non-working area of a steel sample was sealed with epoxy resin and only the work surface was mechanically abraded and polished. A C1018 steel sample was used as the working electrode. The exposed area of these samples was 0.78 cm^2.

All the coupons were ground to P2000 with SiC grit paper, rinsed with acetone, and then dried at room temperature.

Analytical grade 37 wt.% HCl was used for the preparation of the aggressive solution (1 mol·L^{-1} and 5 mol·L^{-1} HCl) for all chemical and electrochemical studies.

2.3. Weight loss measurements

Static weight loss measurements were applied to study the inhibition efficiency of DATT (ΔW, %) on mild steel after immersion at 25°C for 24 hours in 1 M and 5 M HCl.

After weight loss experiments typical profiles of the steel surface were obtained. 3D profile diagrams were examined by a NewView 7300 3D optical profilometer (USA) using a 50x zoom lens. The roughness parameters (R_a and R_z) were calculated over the entire examined surface.

2.4. Electrochemical measurements

The electrochemical measurements were conducted using Solartron electrochemical equipment consisting of a Solartron 1255 frequency response analyzer connected to a Solartron 1287 potentiostat. Experiments were carried out in a traditional three-electrode cell. A silver/silver chloride electrode and a platinum electrode were used as the reference electrode and counter electrode, respectively. Before the electrochemical measurements, the open circuit potential (OCP) was monitored for 1 h.

Potentiodynamic polarization curves were recorded from the cathodic region of potentials, namely, from –200 to +200 mV *versus* OCP at a scan rate of 0.5 mV/s. All potential values are presented *versus* the silver/silver chloride electrode. Polarization measurements were performed at temperature ranging from 293 to 353 K. Temperature was controlled by a LOIP LT 100 thermostat with external circulation.

The electrochemical impedance spectroscopy (EIS) measurements were carried out in the frequency range from 20 kHz to 0.02 Hz using a potential amplitude of ± 5 mV relative to OCP. EIS data was fitted by ZView2 software.

After that, the surface coverage (θ) of the working electrode by the corrosion inhibitor molecules was determined by the equation:

$$\theta = \frac{C_0 - C}{C_0 - C_1}$$

where C_0, C and C_1 are the capacitance of the double electric layer in the pure acid solution, in a solution with some concentration of the inhibitor, and in a solution with $\theta = 1$.

The double-layer capacitance was calculated from the value of the imaginary component of the impedance Z'' at $f = 10$ kHz:

$$C = -\frac{1}{\omega Z''}$$

where ω is the circular frequency of the alternating current ($\omega = 2nf$).

The potentiodynamic curves method (PCM) makes it possible to calculate the corrosion rate i_{corr} (A/m^2) as the corrosion current density at the free corrosion potential, E_{corr} (V), and estimate which of the partial electrode reactions (hydrogen evolution reaction or metal ionization) is mainly hindered by the inhibitor. It is also possible to determine the Tafel slopes, b_c and b_a (mV), and calculate the inhibition percentage, IP (%), as follows:

$$IP = \frac{i_{corr(0)} - i_{corr}}{i_{corr(0)}}$$

where $i_{corr(0)}$ and i_{corr} are the corrosion current densities in the absence and in the presence of inhibitor, respectively.

Moreover, PCM data enable to calculate the activation energy of the corrosion process. In this case, the effect of temperature on current density for concentration polarization or delayed-stage discharges is described by an equation similar to the Arrhenius equation:

$$\ln i = -\frac{E_{ef}}{RT}$$

where E_{ef} is the effective activation energy, J/mol; T is the temperature, K. The tangent of the slope of the straight line in coordinates $\ln i = f(1/T)$ equals $-E_{ef}/R$.

Surface energy

The contact angle was determined by the sessile drop method with a DSA 25E tensiometer (KRUSS). Water and diethylene glycol were used as the test liquids while the droplet diameters ranged from 2 to 3 mm. The free surface energy (SFE) was calculated by the Owens–Wendt–Rabel–Kaelble (OWRK) method as the sum of the dispersion (taking into

account van der Waals interactions of the surface and the test liquid) and polar (dipole interactions and the energy of hydrogen bonds) components.

Quantum chemical calculation

All DFT calculations were carried out using the Orca 4.2.1 software package [15, 16] with PBE0 [17] generalized gradient functional and a predefined amount of exact exchange. To improve energy values, Grimme's dispersion correction [18] with Becke and Johnson damping [19] was applied. Minimally augmented polarized valence triple-zeta basis set ma-def2-TZVP [20, 21] was used both for geometry optimizations and for energy and electronic calculations. The Conductor-like Continuum Polarization Model (C-PCM) [22] was used for water solvation. Semiempirical GFN2-xTB [23] calculations were performed using the xtb program [24].

Within the framework of the density functional theory, the chemical potential (μ) is defined as the negative of electronegativity (χ) [25]:

$$\chi = -\mu = -\left(\frac{\partial E}{\partial N}\right)_{v(r)}$$

and hardness (η) is defined as [26]

$$\eta = \frac{1}{2}\left(\frac{\partial \mu}{\partial N}\right)_{v(r)} = \frac{1}{2}\left(\frac{\partial^2 E}{\partial N^2}\right)_{v(r)}$$

Using the finite difference approximation, global hardness and chemical potential can be approximated as [27]:

$$\eta = \left(\frac{I - A}{2}\right)$$

$$\mu = -\left(\frac{I + A}{2}\right),$$

where I and A are the first vertical ionization potential and electron affinity, respectively, of the chemical system.

Using the Koopmans theorem [28] and setting $I = -E_{HOMO}$ and $A = -E_{LUMO}$, the chemical potential and global hardness can be expressed as:

$$\mu = \left(\frac{E_{LUMO} + E_{HOMO}}{2}\right)$$

$$\eta = \left(\frac{E_{LUMO} - E_{HOMO}}{2}\right),$$

where E_{HOMO} is the energy of the highest occupied molecular orbital and E_{LUMO} is the energy of the lowest unoccupied molecular orbital. The global softness (σ) is the inverse of global hardness and hardness (η) is defined as [26]:

$$\sigma = \frac{1}{\eta} = \left(\frac{\partial N}{\partial \mu} \right)_{v(r)}$$

The global electrophilicity index (ω) was introduced by Yang and Parr [29] and is given by:

$$\omega = \frac{\mu^2}{4\eta}$$

The Fukui function which measures reactivity in a local sense is by far the most important local reactivity index [30]. The Fukui functions can be defined using finite differences of the electronic density. For nucleophilic attack (the addition of an electron to the molecule) of atom i:

$$f_i^+(r) = \rho(N+1) - \rho(N)$$

and similarly for electrophilic attack (the removal of an electron from the molecule):

$$f_i^-(r) = \rho(N) - \rho(N-1),$$

where $\rho(N)$, $\rho(N-1)$, and $\rho(N+1)$ are the densities of the neutral molecule (N), the cation ($N-1$), and the anion ($N+1$), respectively.

An HSAB-based parameter, the fraction of electrons transferred (ΔN), was introduced by Parr [31] to explain the electron transfer from Lewis base B to Lewis acid A for inhibitors and a metal iron. The HSAB-based parameter can be written as:

$$\Delta N = \frac{\chi_A - \chi_B}{2(\eta_A - \eta_B)} = \frac{\Phi - \chi_{inh}}{2(\eta_{Fe} - \eta_{inh})}$$

The typical values for calculated work function Φ of Fe (110) of 4.82 eV and $\eta_{Fe} = 0$ eV have been used for the calculations. If $\Delta N > 0$, transfer from the molecule to the metal surface is favored, and *vice versa*.

3. Results and Discussion

3.1. Weight loss measurements

The weight loss measurement is the simplest experimental method that has high reliability for detecting the inhibitory properties of corrosion inhibitors. Table 2 shows the results of weight loss tests of C1018 steel in 1 M and 5 M hydrochloric acid without an inhibitor and at different concentrations of the inhibitor.

Table 2. The effect of corrosion inhibitor concentration on the weight loss results of C1018 steel in hydrochloric acid solutions.

C_{inh}, g·L^{-1}	CR, g·m^{-2}·h^{-1}	Π, mm·y^{-1}	IE, %
		1 M HCl	
–	2.36±0.14	2.62±0.16	–
0.05	0.81±0.03	0.90±0.04	65.7±2.6
0.1	0.33±0.01	0.37±0.01	86.0±2.6
0.2	0.27±0.01	0.30±0.01	88.6±2.7
		5	
–	15.21±1.06	16.87±1.18	–
0.05	1.32±0.07	1.46±0.07	91.3±4.6
0.1	0.45±0.02	0.50±0.02	97.0±4.9
0.2	0.31±0.01	0.34±0.01	98.0±3.9

According to Table 2, the corrosion rate (*CR*) decreases significantly after adding the inhibitor into the studied corrosion system. Inspection of these data reveals that the inhibition efficiency rises at a higher concentration of DATT. The *IE* in 5 M HCl solution is higher than in 1 M HCl solution. The corrosion inhibition can be explained by the adsorption of thiadiazole molecules at the mild steel/acid solution interface.

Adsorption of DATT is likely to be determined by the heteroatoms (S, N) in the thiadiazole ring of the studied compound and by π-electrons (by resonance structures) in the system of conjugated double bonds.

3.2. Quantum chemical calculation

3.2.1. Protonation of DATT

It is known that tight binding methods reasonably well describe the relative proton affinities (PA) and so they can rank different protonation sites of a molecule (also referred to as protomers). The neutral form of DATT can be represented by at least two tautomeric forms (see Figure 2, a, b). The other three protonation sites of the DATT structure are the three nitrogen atoms (c−e). To identify the most stable protomer, semiempirical calculations using Grimme's GFN2-xTB method with implicit water solvation were performed. As expected, thionic form (b) has the lowest free energy value.
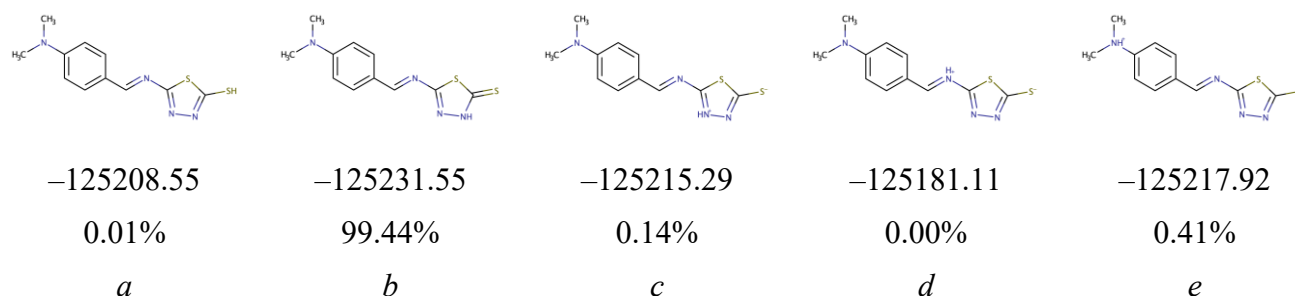
−125208.55	−125231.55	−125215.29	−125181.11	−125217.92
0.01%	99.44%	0.14%	0.00%	0.41%
a	*b*	*c*	*d*	*e*

Figure 2. Tautomeric (a, b) and zwitterionic (c−e) forms of DATT with their Gibbs energy values (kJ·mol^{-1}) at GFN2-xTB[GBSA(water)] level and relative abundances calculated using the Boltzmann distribution (298 K).

The same calculations were performed to find the most stable protomer among mono, double and triple protonated structures. Protomers with the lowest energies are shown in Figure 3. The geometrical parameters of all forms optimized at the PBE0-D3BJ[C-PCM(Water)]/ma-def2-TZVP level of theory are presented in Table 3. All the structures are almost flat, except for the triple protonated form. One can note that the phenyl rings of DATT and its mono- and diprotonated forms are slightly distorted. The C1−C6 and C4−C4 bond length are about 0.1 Å shorter than the C1−C2, C2−C3, C4−C5, and C5−C6 bond lengths. The C2−N7 bond length is also too short for typical single bonds. This distortion can be explained by the formation of a quinoid-like structure with the C2−N7 bond involved in conjugation.
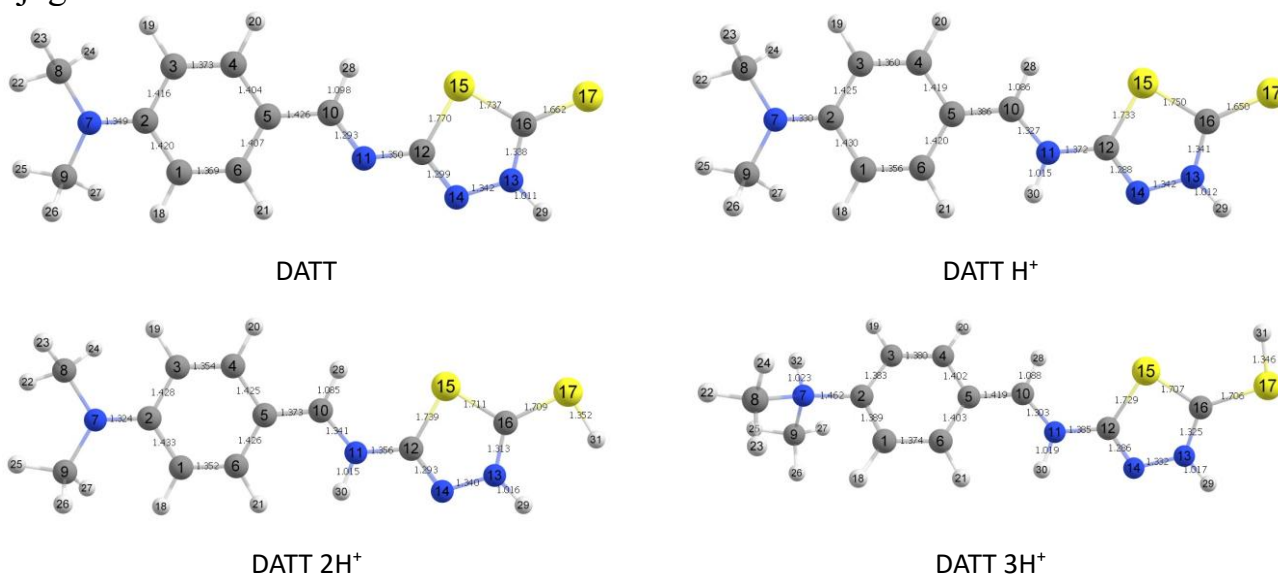

Figure 3. The geometries of DATT and its mono, double, and triple protonated forms optimized at PBE0-D3BJ[C-PCM(Water)]/ma-def2-TZVP level of theory (atoms legend: blue = N; yellow = S; light grey = H, grey = C).

Mono- and diprotonation of DATT extends the conjugation chain to include the C5−C10 bond and increases the intensity of its color. Full protonation breaks this quinoid-like structure with flattened bonds of the phenyl ring, and C2−N7 and C5−C10 are of a typical

single bond length. This result agrees with our experiment: we observed a great improvement of the color intensity of DATT orange crystals during their dissolution in HCl, but the resulting solution is almost colorless.

    Electrostatic interaction between the protonated forms of the molecule and the metal surface is possible only for a negatively charged metal surface. In concentrated HCl solutions, this is achieved by a negatively charged surface layer of chloride ions (Cl⁻) which are first adsorbed onto the positively charged metal surface. Under these conditions, adsorption of positively charged protonated compounds is favored. Oxygen, sulfur and nitrogen atoms with their lone pair electrons define the donor-acceptor interactions and the vacant 3d-orbitals of the iron.

Table 3. Bond length (Å), bond and torsion angles (°) for the optimized molecules of DATT and its protonated forms calculated at the PBE0-D3BJ[C-PCM(Water)]/ma-def2-TZVP level of theory.

Parameter	DATT	DATT H⁺	DATT 2H⁺	DATT 3H⁺	Parameter	DATT	DATT H⁺	DATT 2H⁺	DATT 3H⁺
					Bond length				
C1–C2	1.420	1.430	1.433	1.389	N7–H32				1.023
C2–C3	1.416	1.425	1.428	1.383	S17–H31			1.352	1.347
C3–C4	1.374	1.360	1.354	1.380	N11–H30			1.015	1.019
C4–C5	1.404	1.419	1.425	1.402	N13–H29	1.011	1.012	1.017	1.017
C5–C6	1.407	1.420	1.426	1.403	C16–S17	1.662	1.650	1.709	1.706
C1–C6	1.369	1.356	1.352	1.374	S15–C16	1.737	1.750	1.711	1.707
C2–N7	1.349	1.330	1.325	1.462	C12–S15	1.770	1.733	1.739	1.729
C5–C10	1.426	1.386	1.373	1.419	N13–C16	1.338	1.341	1.313	1.325
C10–N11	1.293	1.327	1.341	1.303	N13–N14	1.342	1.342	1.340	1.332
N11–C12	1.350	1.372	1.356	1.386	C12–N14	1.299	1.288	1.293	1.286
					Bond angle				
∠C1–C2–C3	177.7	118.2	118.3	122.6	∠C4–C5–C6	117.8	118.0	118.0	120.1
∠C2–C3–C4	120.5	120.4	120.3	118.7	∠C5–C6–C1	121.3	121.1	121.0	120.0
∠C3–C4–C5	131.7	121.6	121.5	119.9	∠C6–C1–C2	121.0	120.8	120.8	118.7

    Figure 4 shows the frontier orbitals of different DATT forms. The electronic density of the neutral form, mono-, and double-protonated forms on the highest occupied molecular orbital (HOMO) is delocalized along the whole molecule except for S15 of the thiadiazole ring. This confirms the quinoid-like structure of DATT and its mono- and di-protonated forms. Protonation of N7 shortens the conjugation chain.
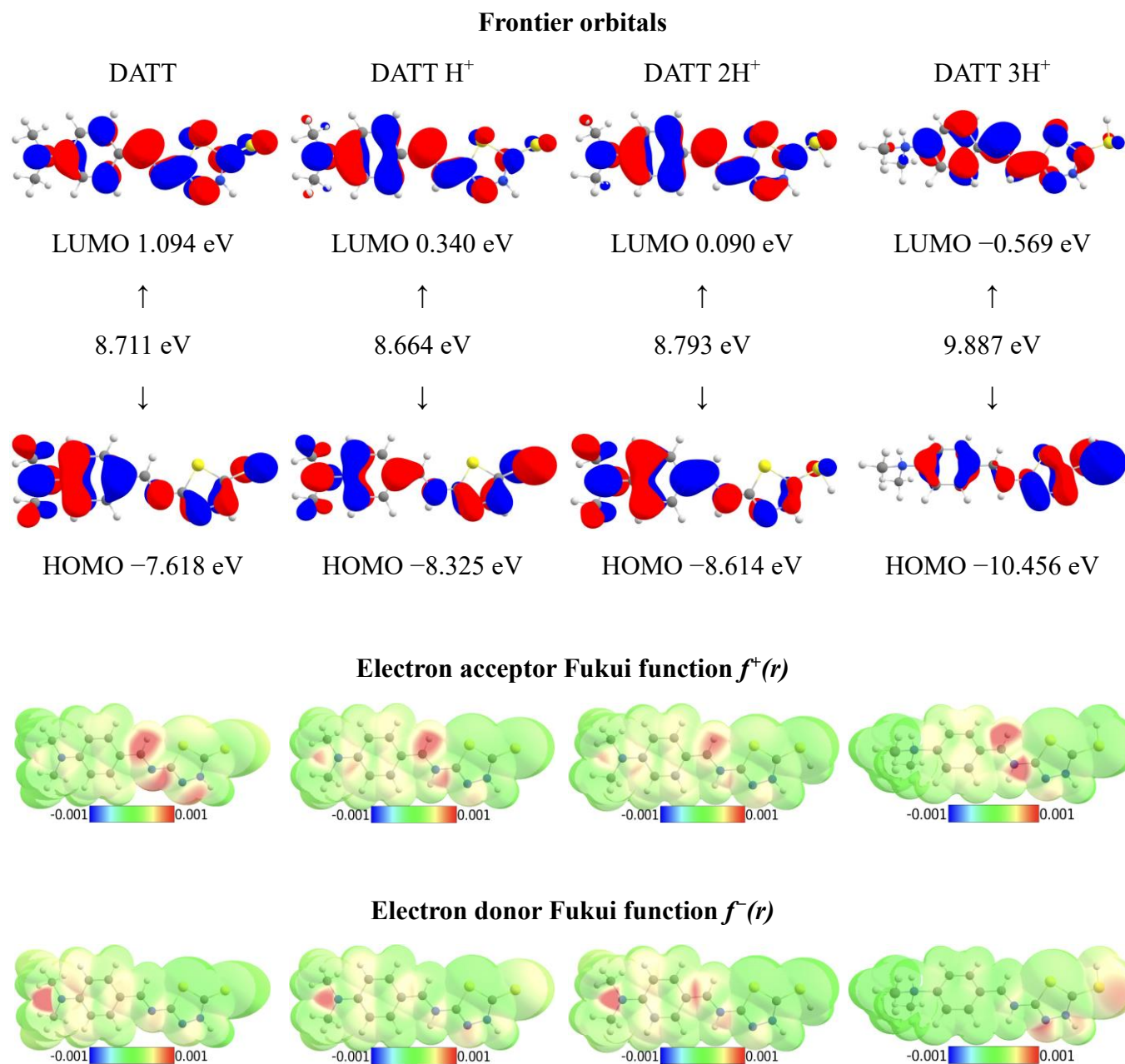
Frontier orbitals

DATT	DATT H$^+$	DATT 2H$^+$	DATT 3H$^+$

LUMO 1.094 eV	LUMO 0.340 eV	LUMO 0.090 eV	LUMO −0.569 eV
↑	↑	↑	↑
8.711 eV	8.664 eV	8.793 eV	9.887 eV
↓	↓	↓	↓

HOMO −7.618 eV	HOMO −8.325 eV	HOMO −8.614 eV	HOMO −10.456 eV

Electron acceptor Fukui function $f^+(r)$

Electron donor Fukui function $f^-(r)$

Figure 4. Frontier orbitals with their respective energies at the PBE0-D3BJ[C-PCM(Water)]/ ma-def2-TZVP//HF[C-PCM(Water)]/ma-def2-TZVP level of theory; electron acceptor f^+ (r) and electron donor f^-(r) Fukui functions mapped on the van der Waals (vdW) surfaces of DATT and its protonated forms at the PBE0-D3BJ[C-PCM(Water)]/ma-def2-TZVP level of theory.

The electronic density of HOMO represents the nucleophilic center of a molecule from which the electron can be transferred to the vacant 3-d orbital of iron. The electrophilic centers of a molecule that accepts electrons transferred *via* back-donation from iron surface is represented by the LUMO electronic density. This center involves the S15 sulfur atom of the thiadiazole ring.

The energy of HOMO and LUMO contributes to the electronic donating and accepting ability of the compound and its protonated forms to/from the atomic orbitals of the metal. The higher E_H and the lower E_L, the higher the adsorption ability and the higher the inhibition efficiency are. One can note that with increasing protonation of DATT, E_H also rises, while E_L goes down keeping the energy gap relatively constant up to the fully protonated form. The fully protonated form of DATT therefore should have the lowest adsorption and inhibition efficiency. The energy gap (ΔE_{L-H}) is an index of reactivity or stability of the inhibitor molecule. Since the value of ΔE_{L-H} is small, the electron polarizability is easy, while in turn, the adsorption efficiency of the tested molecule is high. Protonation of DATT reduces the charge transfer between the inhibitor molecule and the metal surface, meaning that the molecule-to-metal charge transfer is more favorable for all the DATT forms except for the fully protonated one.

Metals are considered as soft acids, while inhibitor molecules are regarded as soft bases. Thus, the soft-soft interaction is the crucial factor for the adsorption of inhibitor molecules. We found that the hardness parameter η and its inverse form S (softness) do not depend on the protonation, except for the fully protonated form which has a bit higher hardness.

The fraction of transferred electrons (ΔN) values calculated show that for all the DATT forms, except for the fully protonated one, the transfer of electrons from the inhibitor molecule to the metal surface is more favorable.

Table 4. Calculated properties of DATT and its protonated forms obtained by HF[C-PCM(Water)]/ma-def2-TZVP calculations.

	E_H (eV)	E_L (eV)	ΔE_{L-H} (eV)	χ (eV)	η (eV)	σ (eV^{-1})	ω (eV)	ΔN
DATT	−7.618	1.093	8.711	3.263	4.356	0.230	0.611	0.179
DATT H$^+$	−8.325	0.340	8.664	3.992	4.332	0.231	0.920	0.096
DATT 2H$^+$	−8.614	0.090	8.793	4.262	4.352	0.230	1.043	0.064
DATT 3H$^+$	−10.452	−0.569	9.887	5.512	4.943	0.202	1.537	−0.079

Mulliken population of DATT and its protonated forms were estimated at the PBE0-D3BJ[C-PCM(Water)]/ma-def2-TZVP level of theory. The results are demonstrated in Table 5. The largest negative charge is obtained for the unprotonated S17 atom and two carbons C8 and C9 of the methyl group. Unprotonated nitrogen atoms of the thiadiazole moiety (N13 and N14) and the N11 atom of the spacer group also have relatively high negative charges that facilitate the protonation of these sites.

Table 5. Mulliken charges for the DATT and its protonated forms calculated at the PBE0-D3BJ[C-PCM(Water)]/ma-def2-TZVP level of theory.

	DATT	DATT H+	DATT 2H+	DATT 3H+
C1	−0.011	−0.119	−0.089	−0.042
C2	0.183	0.154	0.092	−0.066
C3	−0.457	−0.383	−0.332	−0.061
C4	−0.026	0.144	0.138	0.038
C5	−0.086	0.085	0.064	−0.150
C6	−0.283	−0.398	−0.401	−0.246
N7	0.057	0.095	0.134	0.064
C8	−0.427	−0.431	−0.438	−0.330
C9	−0.422	−0.427	−0.436	−0.341
C10	0.140	0.138	0.187	0.185
N11	−0.246	−0.091	−0.101	−0.004
C12	0.097	0.089	0.105	0.101
N13	−0.135	−0.078	−0.036	−0.062
N14	−0.256	−0.251	−0.243	−0.148
S15	−0.019	0.049	0.150	0.154
C16	0.238	0.218	0.235	0.294
S17	−0.607	−0.553	−0.110	−0.073

Donor-acceptor types of interactions are facilitated by the active sites in the inhibitor molecules. Calculation of the condensed Fukui indices is one of the most popular methods to determine these active sites. Figure 4 shows the most electron deficient sites of the molecules favorable for the nucleophilic attacks mapped on the van der Waals surface of the molecule ($f^+(r)$): C10 and N11 atoms of the spacer. The electron rich sites favorable for the electrophilic attacks can be found using $f^-(r)$. These sites include the unprotonated N7 atom of the amino group and N14 with S17 for the fully protonated DATT.

3.3. Potentiodynamic polarization measurements

Figure 5 (a) and (b) show typical polarization curves for a mild steel electrode in 1 M and 5 M HCl, respectively, without and with 0.1 g·L^{-1} DATT at 293 K. A number of polarization tests were performed to estimate the action mechanism of the inhibitor. According to the weight loss experiment, the optimal concentration of the studied substances is 0.10 g·L^{-1}. The curves obtained at 303 K, 313 K, 333 K, and 353 K had similar shapes. That is why only the polarization curves at 293 K are shown. From the plots depicted in Figure 5, it is evident that both anodic and cathodic reactions on the mild steel electrode were inhibited by the

thiadiazole derivative. This result suggests that the addition of DATT reduces the anodic dissolution and suppresses the hydrogen evolution reaction.

Table 6 presents the electrochemical kinetic parameters obtained from the potentiodynamic polarization curves in the range of temperatures (293–353 K). All the observations about the parameters are related to the parameters in the absence of DATT. In both HCl solutions as demonstrated in Table 6, no significant shifts in E_{corr} values were observed in the presence of DATT compared with the E_{corr} value in the blank solutions. As it is reported in literature, if the value of E_{corr} is less than 85 mV with respect to the value obtained in the blank acid solution, the inhibitor is termed as a mixed type inhibitor [32].

Table 6. Electrochemical kinetic parameters obtained from potentiodynamic polarization curves for a mild steel electrode in 1 and 5 M HCl without and with 0.1 g·L^{-1} DATT in the temperature range of 293–353 K.

Inhibitor	T, K	b_a, mV	b_c, mV	$i_{corr} \cdot 10^4$, A·m^2	$-E_{corr}$, mV	$Z_{el/chem}$, %
				1M HCl		
–	293	65	141	0.92	434	–
DATT		149	107	0.43	447	53
–	303	66	141	1.03	434	–
DATT		106	112	0.48	447	53
–	313	67	146	1.49	443	–
DATT		99	107	0.57	429	58
–	333	70	158	3.37	436	–
DATT		67	105	1.72	428	60
–	353	62	163	2.41	412	–
DATT		20	110	9.02	430	73
				5 M HCl		
–	293	93	140	15.8	400	–
DATT		200	122	0.25	485	84
–	303	74	148	2.01	397	–
DATT		178	122	0.27	479	85
–	313	62	154	3.16	390	–
DATT		167	122	0.31	470	84
–	333	55	167	5.01	380	–
DATT		153	122	0.33	460	90
–		20	182	199.50	320	–
DATT		50	125	0.89	415	99

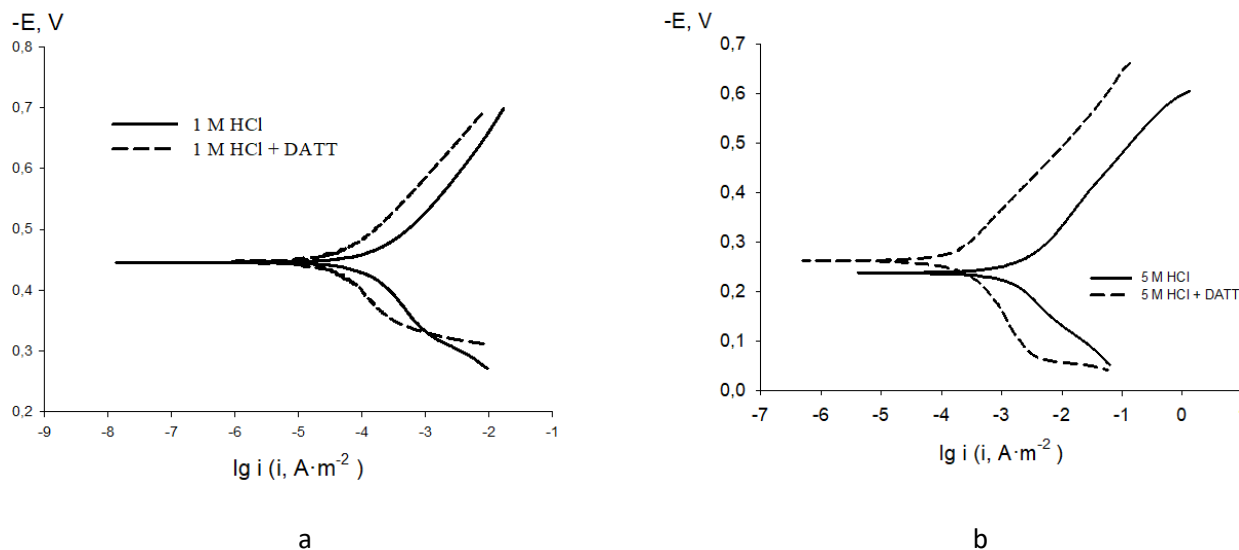**Figure 5.** Potentiodynamic polarization curves of the mild steel electrode in 1 (a) and 5 M (b) HCl without and with 0.1 g·L^{-1} DATT.

In 1 M and 5 M HCl, the Tafel coefficients b_c change in the same way when DATT is added to the corrosion system (a decrease by 20–60 mV). However, the Tafel coefficients b_c in 1 M grow in the temperature range of 293–353 K by a factor of 1.5–2, then decrease, while in 5 M solution they grow by a factor of 2–2.5. However, the inhibitor efficiency is determined by the metal dissolution as well as hydrogen evolution. In our case, the anodic dissolution reaction controls the process, thereby reducing the overall corrosion rate [33].

Moreover, Table 6 illustrates that the corrosion current density with DATT decreased as compared with the pure HCl solution. The inhibitor efficiency correlated with the weight loss experiments at room temperature; it decreased with temperature in 1 M HCl and increased in 5 M HCl.

3.4. Electrochemical impedance spectroscopy study

Figure 7 shows the Nyquist plots for C1018 mild steel in HCl solutions at E_{corr} without DATT and with its different concentrations. The impedance spectra for C1018 in 5 M HCl solutions at E_{corr} are a combination of two semicircles: a capacitive arc in the high-frequency range and an inductive arc in the low-frequency range, but in 1 M HCl solutions there is no inductive arc in both cases. The diameter of the capacitive semicircle increased with an increase in the inhibitor concentration in the solution. This fact can probably be explained by the difficulties in the electrode reactions. To simulate the corrosion-electrochemical behavior of the C1018 electrode in 5 M HCl solutions, we used the equivalent electrical circuit given in Figure 6. In contrast, to simulate the process in 1 M HCl solution, the equivalent electrical circuit has no the $-R_2-L-$ part. The parameter values of the equivalent schemes are shown in Table 7. The values of the χ^2 parameter for the circuits calculated in ZView2 were in the range of $(2-6)\cdot 10^{-4}$, which indicates a good correlation with

experimental data. Moreover, there is a sequential growth in R_1 and R_2 resistances and a decrease in the Q_1 parameter of the constant phase element CPE_1 (at comparable p_1) with an increase in the concentration of DATT. The Q parameter simulates the capacitance of the double electric layer, hence its decrease within one acid concentration indicates that the rate of electrode processes decreases due to blocking of the surface by inhibitor molecules. The R_2 element refers to directly the impedance of the corrosion reaction. As a result, it was concluded that it is sufficient to expand the model with additional resistance and inductance in parallel to the double layer capacitance to account for the penetration of corrosion products to the steel surface.

Table 7. Numerical values of parameters of equivalent circuits for C1018 electrode in HCl solutions without and in the presence of the inhibitor.

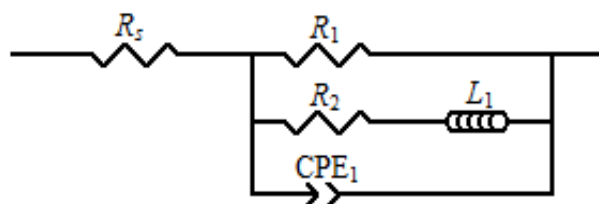| C_{inh}, g·L^{-1}	R_{ct}, Ω·cm^2	R, Ω·cm^2	CPE_1, µF·cm^{-2}·s$^{(p-1)}$		L, H·cm^2	θ
			Q	p		
			1 M HCl			
-	293.2	-	0.71	0.81	-	-
0.01	318.4	-	0.23	0.87	-	0.68
0.05	430.5	-	0.35	0.83	-	0.69
0.10	600.7	-	0.55	0.88	-	0.78
0.20	612.5	-	0.36	0.80	-	0.81
			5 M HCl			
-	31.97	389.4	1.92	0.83	0.000195	-
0.01	41.74	250.0	0.90	0.88	523.0000	0.56
0.05	61.98	397.8	0.76	0.87	1012.000	0.93
0.10	110.80	762.5	0.75	0.88	1466.000	0.94
0.20	123.50	1409.0	0.71	0.87	2231.000	0.98

Figure 6. Equivalent electrical circuit for a C1018 electrode in 5 M HCl solutions at E_{corr}.
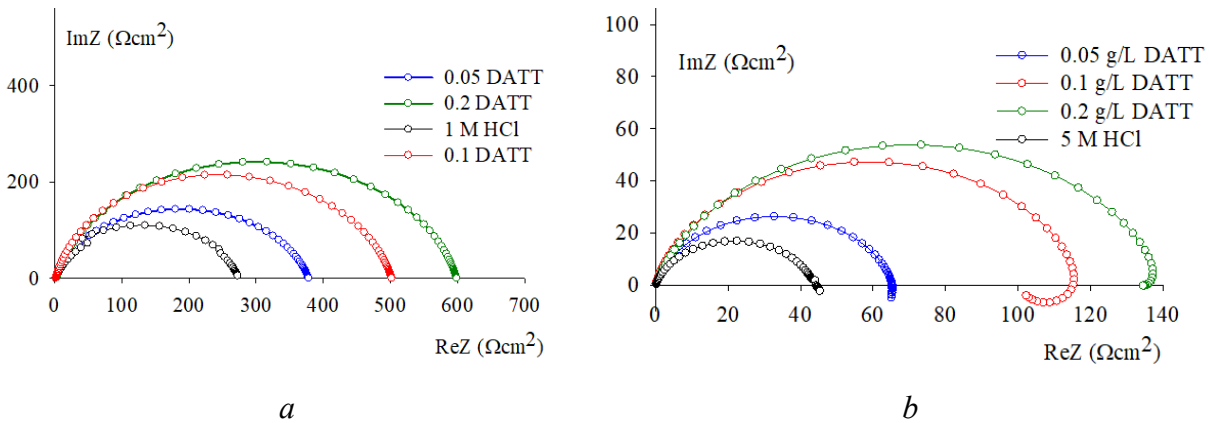
Figure 7. Nyquist impedance plot for mild steel in 1 (a) and 5 M (b) HCl solution in the absence and in the presence of different DATT concentrations.

Table 6 shows the electrochemical kinetic parameters obtained from potentiodynamic polarization curves for a mild steel electrode in 1 and 5 M HCl without and with 0.1 g·L^{-1} DATT in the range of temperatures (293–353 K). As it would be expected, both anodic and cathodic corrosion reactions on a mild steel electrode were inhibited by the presence of DATT in the entire temperature range. This result suggests that addition of DATT reduces the anodic dissolution and also suppresses the hydrogen evolution reaction. Based on the electrochemical parameters (Table 8), Arrhenius plots of lg$i$ *vs.* 1/T obtained are straight lines with a slope of $E_a/2.303R$. Table 8 shows the values of activation energy of the corrosion process.

Table 8. Effective activation energy values for the corrosion process on mild steel in 1 and 5 M HCl without and with 0.1 g·L^{-1} DATT.

Inhibitor	E_{ef}, kJ·mol^{-1}
1 M HCl	
DATT	21.8±1.2
	67.4±1.9
5 M HCl	
DATT	55.4±1.6
	14.6±1.2

3.5. Surface activity at the liquid–gas and liquid–liquid interfaces

The optimal inhibitor concentration is derived from the value of the critical concentration for micelle formation. DATT can be used in the oil industry as an inhibitor against acid corrosion, therefore we try to study the inhibitor's behavior at the interface of hydrocarbons and its acidic solutions. Table 9 shows the results of determining the surface tension at the

liquid–gas and liquid–liquid interface for hydrochloric acid solutions containing different concentrations of DATT.

According to the data obtained, neither the acid concentration nor the concentration of the inhibitor affects the surface tension at the interface between the acidic solutions of DATT and air and the acidic solutions of DATT and octane, *i.e.*, the compound is an inactive surfactant at both interfaces.

Table 9. The surface tension at the interface between hydrochloric acid solutions of DATT and air or octane.

C_{inh}, g·L^{-1}	γ_{LG}, mJ·m^{-2}	γ_{LL}, mJ·m^{-2}
1 M HCl		
–	70.0	12.8
0.05	70.0	12.3
0.10	69.7	12.1
0.20	69.7	11.8
5 M HCl		
–	70.2	12.5
0.05	70.0	12.3
0.10	69.8	11.8
0.20	69.8	11.6

3.6. Contact angle measurement

In recent times, contact angle measurements were also used to detect the corrosion inhibition ability of molecules adsorbing on metal surfaces. When any organic molecules adhere to surfaces consisting of metal atoms, it not only alters the chemical composition of the metal surface but also modifies the profile of the latter. Consequently, the wetting behavior of the metal surface changes due to the structural features and adsorption ability of the inhibitor molecules adsorbed on the surface. Therefore, the inhibitor activity at the solid–liquid interface was investigated by estimating the characteristics of mild steel surfaces wetted by hydrochloric acid solutions of DATT. The results are presented in Figure 8.

According to the data above, the presence of DATT increases the adhesion of the inhibitor molecules to the surface of steel.

The equilibrium of a droplet on a surface can be characterized by parameters such as surface tension at the solid–gas, solid–liquid, and liquid–gas interface and the contact angle:

$$\gamma_{SG} = \gamma_{SL} + \gamma_{LG} \cdot \cos\theta$$

Since the value of γ_{SG} is constant in our case and the values of γ_{LG} were determined firstly, we can indirectly estimate the change in the energy state of the surface as a result of contact with an inhibitor.

Therefore, for an uninhibited solution:

$$\gamma_{SG} = \gamma_{SL}^{0} + \gamma_{LG}^{0} \cos\theta^{0}$$

For an inhibited solution:

$$\gamma_{SG} = \gamma_{SL}^{inh} + \gamma_{LG}^{inh} \cos\theta^{inh}$$

Then, the change in surface energy associated with the formation of the inhibitor film will be:

$$\gamma_{SL}^{0} - \gamma_{SL}^{inh} = \gamma_{LG}^{inh} \cos\theta^{inh} - \gamma_{LG}^{0} \cos\theta^{0}$$
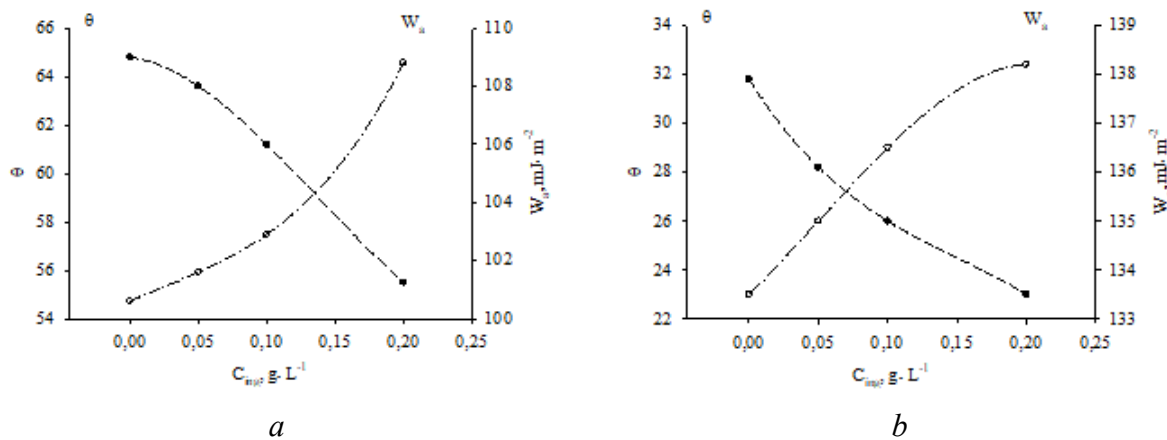
The results of these calculations are given in Table 10.

Figure 8. Isotherms of the contact angle and adhesion of 1 M (a) and 5 M (b) HCl with the added inhibitor.

Table 10. Surface tension in the system C1018 – HCl.

C_{inh}, g·L^{-1}	γ_{LG}^{0}, mJ·m^{-2}	$\cos\theta$	$\gamma_{SL}^{0} - \gamma_{SL}^{inh}$, mJ·m^{-2}
		1 M HCl	
–	70.0	0.425	–
0.05	70.0	0.444	1.1
0.10	69.7	0.481	1.3
0.20	69.7	0.566	9.6
		5 M HCl	
–	70.2	0.851	–
0.05	70.0	0.880	2.0
0.10	69.8	0.897	3.2
0.20	69.8	0.919	4.8

Positive values of $\delta(\gamma_{SL}^0 - \gamma_{SL}^{inh})$ and their increase with the inhibitor concentration indicate a change in the state of the C1018 surface. In our case, it can only be caused by the adsorption of a hydrophobic film of DATT on the steel surface.

3.7. Contact angle measurement and the OWRK method for estimation of the surface condition of steel after a corrosion experiment

There are some factors that influence the efficiency of an inhibitor: the action of the functional groups associated with the aromatic rings of the molecule, the chemical changes occurring in the inhibitor, the chemical nature and surface charge of the metal, and the type of corrosive environment. The main process of the inhibition by these organic compounds is usually the adsorption of inhibitor particles on the metal surface. The dispersion function is often described as the reaction center of the adsorption process, and the adsorption bond strength is determined by the electron density and polarizability of the functional group.

Table 11. Contact angles of test liquids on C1018 surfaces after exposure to the inhibitor and corrosive medium.

C_{inh}, g·L^{-1}	Test liquid	
	Water	Diethylene glycol
	θ, deg	θ, deg
Surface before the experiment		
–	64.8±1.9	57.7±0.6
1 M HCl		
–	32.6±6.5	14.0±2.8
0.05	34.8±4.7	16.9±2.2
0.10	80.9±6.6	17.9±3.7
0.20	80.1±8.9	21.1±2.9
5 M HCl		
–	25.7±6.8	13.0±2.3
0.05	20.6±0.8	14.1±0.6
0.10	23.8±1.7	14.2±1.9
0.20	25.1±1.6	12.8±1.5

In this work, we extended the contact angle method to study surface changes under the action of the inhibitor and corrosive medium. Herein, the wetting characteristics of mild steel surfaces were analyzed as follows: after the weight loss tests, the samples were removed,

washed with distilled deionized water, dried with a stream of hot air and the contact angles were then measured.

The contact angles of steel corroded in the uninhibited solution decrease in both test liquids (water and diethylene glycol). Firstly, this fact is very likely to be due to an increased surface area, as the contact angle of the freshly polished sample was much smaller with the same test liquids. Yet another reason for the increased wetting was the presence of hydrophilic corrosion products.

All the measured contact angles are presented in Table 11. In contrast, the mild steel samples retrieved from 1 M HCl solution containing 0.1 g·L^{-1} DATT demonstrated an increase in the contact angles of water after corrosion experiment since a hydrophobic protective film was formed. The wetting isotherm of water is shown in Figure 9 (curve 1).

On the one hand, surface hydrophobization is not achieved in the 5 M HCl solution (Figure 9, curve 2) due to an increasing surface area and surface roughness, which is confirmed by surface profile diagrams (Figure 10). On the other hand, adsorption of the protonated forms of the inhibitor molecule bearing a positive charge onto the surface of C1018 steel can explain the complete hydrophobization. It is also confirmed by the results of our quantum-chemical calculations. The surface of steel became more homogeneous due to inhibitor action since the standard deviations of contact angles decreased.
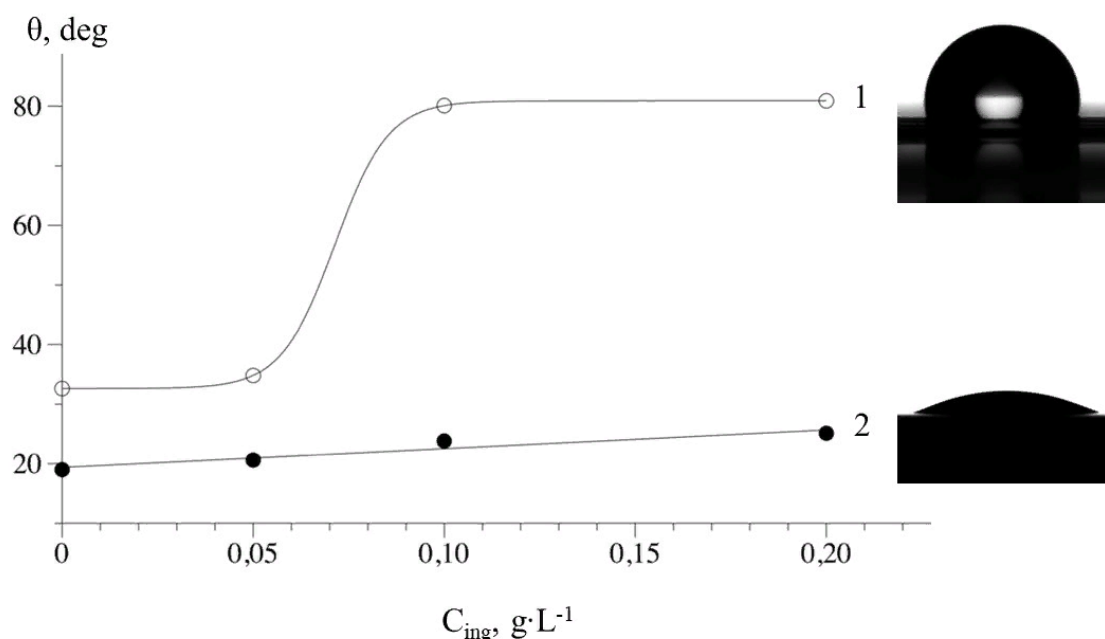
Figure 9. Isotherm of the contact angles of water on the inhibited surface: 1 – 1 M HCl; 2 – 5 M HCl.

The roughness parameters R_a and R_z of steel before immersion were 10 ± 2 nm and 12 ± 3 nm, respectively. The values of roughness parameters after the weight loss experiments increased (Table 12). It should be noted that the R_a and R_z parameters describe only a common tendency of increasing roughness as an integral characteristic of the corrosion process [34, 35]. These parameters can be used where steel surface only undergoes uniform corrosion and there is no localized breakdown or pitting. Both parameters decreased when DATT was added to the corrosion system (Table 12); the surface roughness stabilized and the localization of corrosion processes became less pronounced. However, full stabilization could not be achieved.
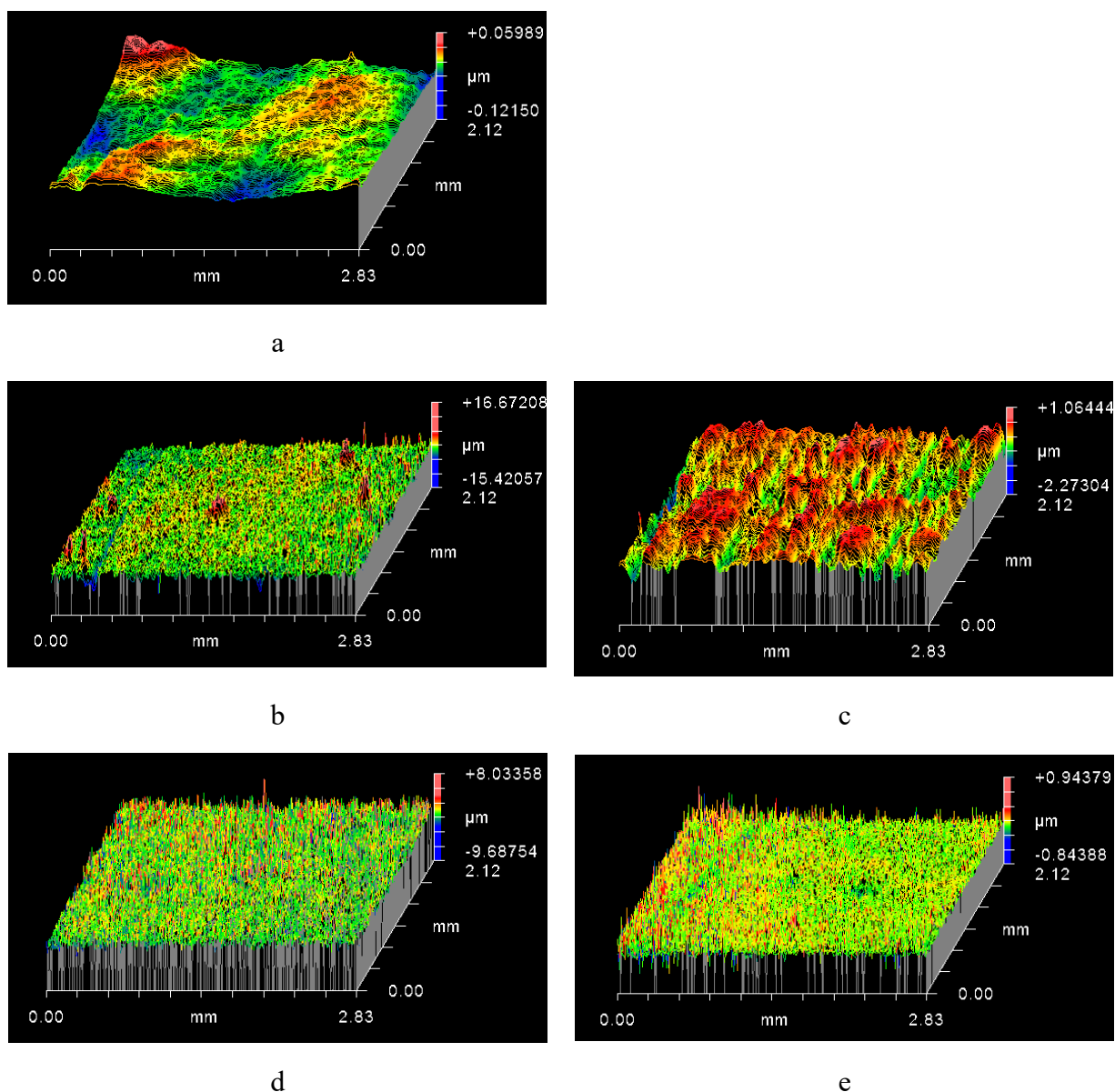
Figure 10. 3D profile diagrams of the C1018 steel surface: a) before the experiment; b, c) after immersion in 1 M and 5 M HCl; d, e) after immersion in 1 M and 5 M HCl with 0.1 g·L^{-1} DATT (immersion time 24 h).

Table 12. Roughness parameters of C1018 steel surface.

Medium	–		DATT, 0.1 g·L^{-1}	
	R_a	R_z	R_a	R_z
	nm			
1 M HCl	292±10	1326±21	46±7	456±10
5 M HCl	1120±18	25220±27	797±10	15354±12

Such a controversial situation made us apply the OWRK method to determine the components of free surface energy (SFE). The results of the calculations are presented in Table 13.

Table 13. Effect of inhibition on SFE values and components.

C_{inh}, g·L^{-1}	γ_{SG}^{d} , mJ·m^{-2}	γ_{SG}^{p} , mJ·m^{-2}	γ_{SG} , mJ·m^{-2}
Polished surface			
–	5.95	31.92	37.88
1 M HCl			
–	9.49	54.02	63.51
0.05	9.65	51.10	61.75
0.10	47.33	1.93	49.27
0.20	44.36	2.56	46.92
5 M HCl			
–	6.40	67.86	74.26
0.05	7.00	64.65	71.65
0.10	17.99	31.34	49.33
0.20	18.38	30.62	49.00

The redistribution of SFE components is a compelling argument for the existence of the protective film and its shielding effect. This redistribution is illustrated in the column diagrams (Figure 11 a, b).

A sharp decrease in the energy component responsible for polar interactions in the corrosive medium/C1018 surface system and an increase in the dispersion component due to the formation of protective DATT film leads to significant inhibition of the corrosion process and causes the high protective effect of the inhibitor (Figure 11 c, d).
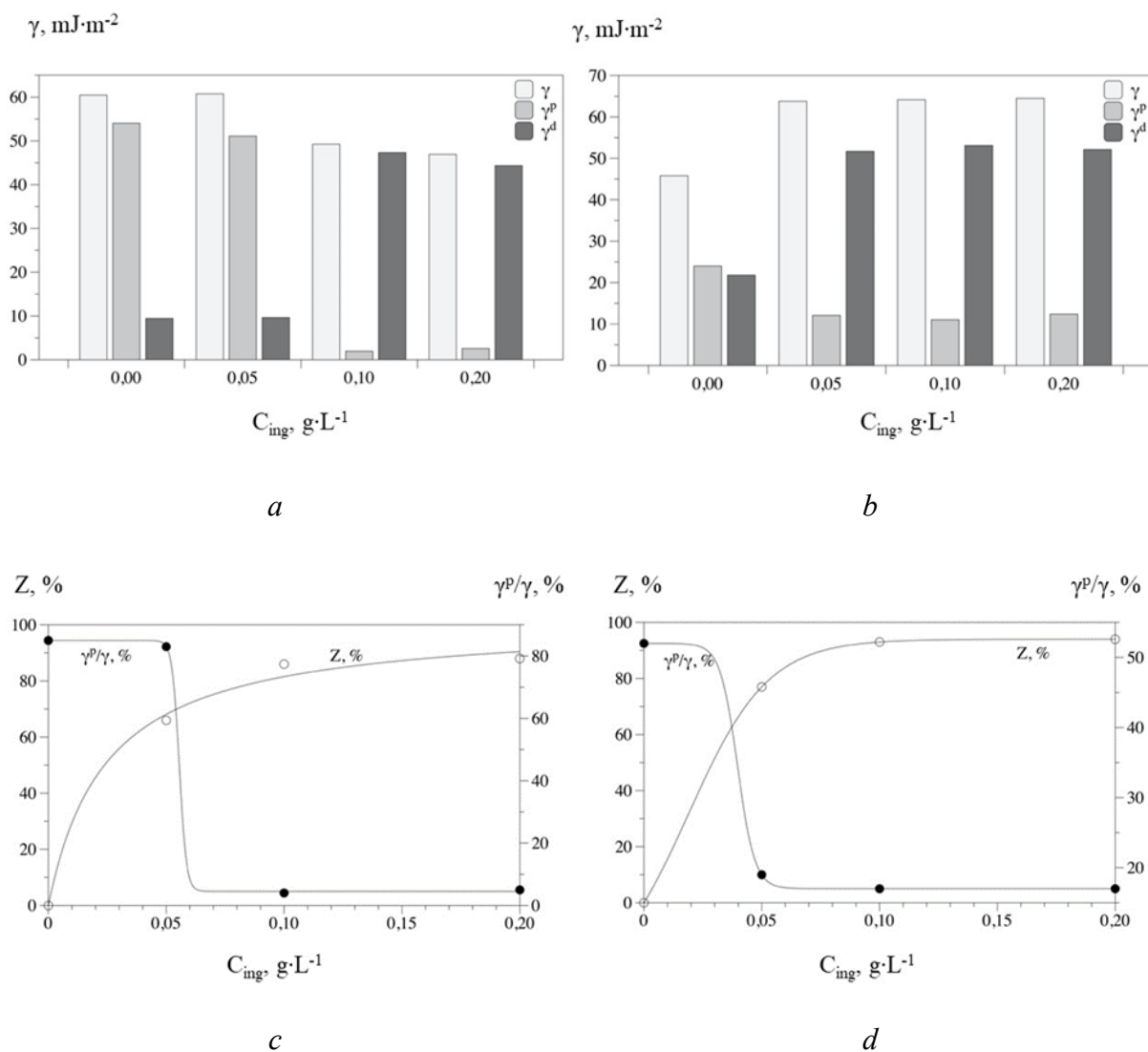
Figure 11. Variation of SFE components (a, b) and its correlation with the protective effect (c, d) of DATT in 1 M (a, c) and 5 M HCl (b, d) solutions.

Conclusion

(*E*)-5-{[4(Dimethylamino)benzylidene]amino}-1,3,4-thiadiazole-2-thiol (DATT) acts as an effective inhibitor of acid corrosion for C1018 mild steel. It exhibits a mixed effect and reduces the rates of partial cathodic and anodic reactions. The mechanism of its action changes with an increase in temperature, which can be proven by a sharp increase in the b_c coefficient in the Tafel equation. At the same time, the free corrosion potential shifts in the cathodic direction. Analysis of the polarization curves correlates with the results obtained by impedance spectroscopy. They mostly confirm the cathodic mechanism of the inhibitors' action. Analysis of the impedance spectra shows that the inhibitor's efficiency increases with a growth in concentration and surface coverage. The calculated activation energy values show that the corrosion process slows down due to the physical adsorption of DATT on the

steel surface in 1 M HCl solutions. Measurements of different types are correlate qualitatively. The ability of the DATT molecule to be adsorbed on the steel surface varies with the protonation position of the nitrogen atom. Contact angle results detected protective adsorption films on the steel surface. The nature of adsorption changes from physical to chemical with an increase in the acid concentration, as evidenced by a decrease in the activation energy values.

Acknowledgments

References

1. M.M. Solomon, I.E. Uzoma, J.A.O. Olugbuyiro and O.T. Ademosun, A Censorious Appraisal of the Oil Well Acidizing Corrosion Inhibitors, *J. Pet. Sci. Eng.*, 2022, **215**, 110711. doi: 10.1016/j.petrol.2022.110711

2. D. Wang, Y. Li, B. Chen and L. Zhang, Novel Surfactants as Green Corrosion Inhibitors for Mild Steel in 15% HCl: Experimental and Theoretical Studies, *Chem. Eng. J.*, 2020, **402**, 126219. doi: 10.1016/j.cej.2020.126219

3. B. El-Haitout, I. Selatnia, H. Lgaz, M.R. Al-Hadeethi, H.-S. Lee, A. Chaouiki, Y.G. Ko, I.H. Ali and R. Salghi, Exploring the Feasibility of New Eco-Friendly Heterocyclic Compounds for Establishing Efficient Corrosion Protection for N80 Steel in a Simulated Oil Well Acidizing Environment: From Molecular-Level Prediction to Experimental Validation, *Colloids Surf. A*, 2023, **656**, 130372. doi: 10.1016/j.colsurfa.2022.130372

4. B.D.B. Tiu and R.C. Advincula, Polymeric Corrosion Inhibitors for the Oil and Gas Industry: Design Principles and Mechanism, *React. Funct. Polym.*, 2015, **95**, 25–45. doi: 10.1016/j.reactfunctpolym.2015.08.006.

5. A.H. Alamri, Localized Corrosion and Mitigation Approach of Steel Materials Used in Oil and Gas Pipelines – An Overview, *Eng. Failure Anal.*, 2020, **116**, 104735. doi: 10.1016/j.engfailanal.2020.104735

6. D.S. Chauhan, M.A.J. Mazumder, M.A. Quraishi and K.R. Ansari, Chitosan-Cinnamaldehyde Schiff Base: A Bioinspired Macromolecule as Corrosion Inhibitor for Oil and Gas Industry, *Int. J. Biol. Macromol.*, 2020, **158,** 127–138. doi: 10.1016/j.ijbiomac.2020.04.200

7. S. Şafak, B. Duran, A. Yurt and G. Türkoğlu, Schiff Bases as Corrosion Inhibitor for Aluminium in HCl Solution, *Corros. Sci.*, 2012, **54,** 251–259. doi: 10.1016/j.corsci.2011.09.026

8. F.E.-T. Heakal and A.E. Elkholy, Gemini Surfactants as Corrosion Inhibitors for Carbon Steel, *J. Mol. Liq.*, 2017, **230**, 395–407. doi: 10.1016/j.molliq.2017.01.047

9. M. Farsak, H. Keleş and M.A. Keleş, New Corrosion Inhibitor for Protection of Low Carbon Steel in HCl Solution, *Corros. Sci.*, 2015, **98**, 223–232. doi: 10.1016/j.corsci.2015.05.036

10. M.N. El-Haddad, Chitosan as a Green Inhibitor for Copper Corrosion in Acidic Medium, *Int. J. Biol. Macromol*., 2013, **55**, 142–149. doi: 10.1016/j.ijbiomac.2012.12.044

11. M.N. El-Haddad, Hydroxyethylcellulose Used as an Eco-Friendly Inhibitor for 1018 c-Steel Corrosion in 3.5% NaCl Solution, *Carbohydr. Polym*., 2014, **112**, 595–602. doi: 10.1016/j.carbpol.2014.06.032

12. A. Dehghani, G. Bahlakeh, B. Ramezanzadeh and M. Ramezanzadeh, Potential Role of a Novel Green Eco-Friendly Inhibitor in Corrosion Inhibition of Mild Steel in HCl Solution: Detailed Macro/Micro-Scale Experimental and Computational Explorations, *Constr. Build. Mater*., 2020, **245**, 118464. doi: 10.1016/j.conbuildmat.2020.118464

13. M.D. Plotnikova, A.D. Solovyev, A.B. Shein, A.N. Vasyanin and A.S. Sofronov, Corrosion Inhibition of Mild Steel by Triazole and Thiadiazole Derivatives in 5 M Hydrochloric Acid Medium, *Int. J. Corros. Scale Inhib*., 2021, **10**, no. 3, 1336–1354. doi: 10.17675/2305-6894-2021-10-3-29

14. M.D. Plotnikova, A.B. Shein, M.G. Shcherban' and A.D. Solovyev, The Study of Thiadiazole Derivatives as Potential Corrosion Inhibitors of Low-Carbon Steel in Hydrochloric Acid, *Bull. Univ. Karaganda Chem*., 2021, **103**, no. 3, 93–102. doi: 10.31489/2021Ch3/93-102

15. F. Neese, The ORCA Program System, *WIREs Comput. Mol. Sci*., 2012, **2**, no. 1, 73–78. doi: 10.1002/wcms.81

16. F. Neese, Software Update: The ORCA Program System, Version 4.0, *WIREs Comput. Mol. Sci*., 2018, **8**, no. 8. doi: 10.1002/wcms.1327

17. C. Adamo and V. Barone, Toward Reliable Density Functional Methods without Adjustable Parameters: The PBE0 Model, *J. Chem. Phys*., 1999, **110**, no. 13, 6158–6170. doi: 10.1063/1.478522

18. S. Grimme, J. Antony, S. Ehrlich and H.A. Krieg, Consistent and Accurate *Ab Initio* Parametrization of Density Functional Dispersion Correction (DFT-D) for the 94 Elements H-Pu, *J. Chem. Phys*., 2010, **132**, no. 15, 154104. doi: 10.1063/1.3382344

19. S. Grimme, S. Ehrlich and L. Goerigk, Effect of the Damping Function in Dispersion Corrected Density Functional Theory, *J. Comput. Chem*., 2011, **32**, no. 7, 1456–1465. doi: 10.1002/jcc.21759

20. F. Weigend and R. Ahlrichs, Balanced Basis Sets of Split Valence, Triple Zeta Valence and Quadruple Zeta Valence Quality for H to Rn: Design and Assessment of Accuracy, *Phys. Chem. Chem. Phys*., 2005, **7**, no. 18, 3297. doi: 10.1039/b508541a

21. J. Zheng, X. Xu and D.G. Truhlar, Minimally Augmented Karlsruhe Basis Sets, *Theor. Chem. Acc*., 2011, **128**, no. 3, 295–305. doi: 10.1007/s00214-010-0846-z

22. V. Barone and M. Cossi, Quantum Calculation of Molecular Energies and Energy Gradients in Solution by a Conductor Solvent Model, *J. Phys. Chem. A*, 1998, **102**, no. 11, 1995–2001. doi: 10.1021/jp9716997

23. C. Bannwarth, S. Ehlert and S. Grimme, GFN2-XTB – An Accurate and Broadly Parametrized Self-Consistent Tight-Binding Quantum Chemical Method with Multipole

Electrostatics and Density-Dependent Dispersion Contributions, *J. Chem. Theory Comput.*, 2019, **15**, no. 3, 1652–1671. doi: 10.1021/acs.jctc.8b01176

24. C. Bannwarth, E. Caldeweyher, S. Ehlert, A. Hansen, P. Pracht, J. Seibert, S. Spicher and S. Grimme, Extended tight-binding Quantum Chemistry Methods, *WIREs Comput. Mol. Sci.*, 2021, **11**, 2. doi: 10.1002/wcms.1493

25. H. Chermette, Chemical Reactivity Indexes in Density Functional Theory, *J. Comput. Chem.*, 1999, **20**, no. 1, 129–154. doi: 10.1002/(SICI)1096-987X(19990115)20:1<129::AID-JCC13>3.0.CO;2-A

26. R.G. Parr and P.K. Chattaraj, Principle of Maximum Hardness, *J. Am. Chem. Soc.*, 1991, **113**, no. 5, 1854–1855. doi: 10.1021/ja00005a072

27. R.P. Iczkowski and J.L. Margrave, Electronegativity, *J. Am. Chem. Soc.*, 1961, **83**, no. 17, 3547–3551. doi: 10.1021/ja01478a001

28. T. Koopmans, Über die Zuordnung von Wellenfunktionen und Eigenwerten zu den Einzelnen Elektronen Eines Atoms, *Physica*, 1934, **1**, no. 3, 104–113. doi: 10.1016/S0031-8914(34)90011-2

29. R.G. Parr, L.V. Szentpály and S. Liu, Electrophilicity Index, *J. Am. Chem. Soc.*, 1999, **121**, no. 9, 1922–1924. doi: 10.1021/ja983494x

30. K. Fukui, Role of Frontier Orbitals in Chemical Reactions, *Science*, 1982, **218**, no. 4574, 747–754. doi: 10.1126/science.218.4574.747

31. R.G. Parr and R.G. Pearson, Absolute Hardness: Companion Parameter to Absolute Electronegativity, *J. Am. Chem. Soc.*, 1983, **105**, no. 26, 7512–7516. doi: 10.1021/ja00364a005

32. T.K. Chaitra, K.N.S. Mohana and H.C. Tandon, Thermodynamic, Electrochemical and Quantum Chemical Evaluation of Some Triazole Schiff Bases as Mild Steel Corrosion Inhibitors in Acid Media, *J. Mol. Liq.*, 2015, **211**, 1026–1038. doi: 10.1016/j.molliq.2015.08.031

33. S. Varvara, L.M. Muresan, K. Rahmouni and H. Takenouti, Evaluation of Some Non-Toxic Thiadiazole Derivatives as Bronze Corrosion Inhibitors in Aqueous Solution, *Corros. Sci.*, 2008, **50**, no. 9, 2596–2604. doi: 10.1016/j.corsci.2008.06.046

34. L.A. Khamaza, Generalized Diagram of the Ultimate Nominal Stresses (Endurance Limit) and the Corresponding Dimensions of the Non-Propagating Fatigue Cracks for Sharp and Blunt Notches, *Strength Mater.*, 2019, **51**, no. 3, 350–360. doi: 10.1007/s11223-019-00081-w

35. Yu.G. Matvienko, Approaches of Fracture Mechanics in the Analysis of Admissible Defects in the Form of Notches, *Strength Mater.*, 2010, **42**, no. 1, 58–63. doi: 10.1007/s11223-010-9188-2

♦ ♦ ♦